- Supplemental Material -

Quantitative Disentanglement of Spin Seebeck, Proximity-Induced, and Ferromagnet-Induced Anomalous Nernst Effect in Normal-Metal–Ferromagnet Bilayers

Panagiota Bougiatioti[1], Christoph Klewe[1,2], Daniel Meier[1], Orestis Manos[1], Olga Kuschel[3], Joachim Wollschläger[3],
Laurence Bouchenoire[4,5], Simon D. Brown[4,5], Jan-Michael Schmalhorst[1], Günter Reiss[1], and Timo Kuschel[1,6]
[1] *Center for Spinelectronic Materials and Devices, Department of Physics,*
Bielefeld University, Universitätsstraße 25, 33615 Bielefeld, Germany
[2] *Advanced Light Source, Lawrence Berkeley National Laboratory, Berkeley, CA 94720, USA*
[3] *Department of Physics and Center of Physics and Chemistry of New Materials,*
Osnabrück University, Barbarastrasse 7, 49076 Osnabrück, Germany
[4] *XMaS, European Synchrotron Radiation Facility, Grenoble, 38043, France*
[5] *Department of Physics, University of Liverpool, Liverpool L69 7ZE, UK*
[6] *Physics of Nanodevices, Zernike Institue for Advanced Materials,*
University of Groningen, Nijenborgh 4, 9747 AG Groningen, The Netherlands

(Dated: November 17, 2017)

I. SAMPLE FABRICATION AND CHARACTERIZATION

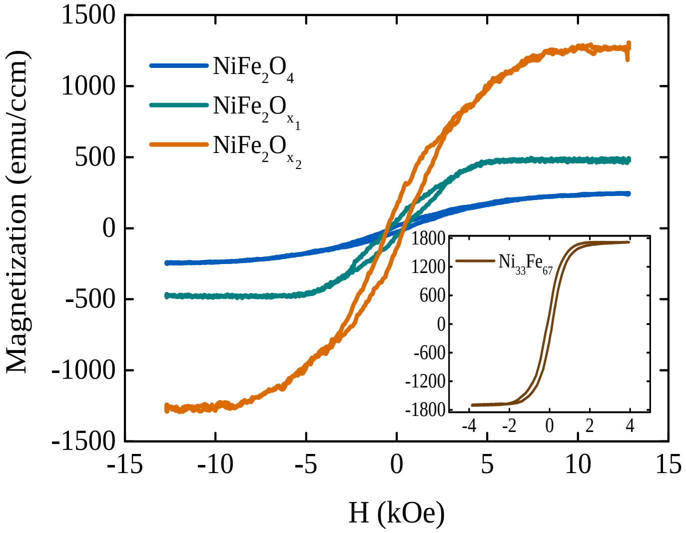

FIG. S 1. Magnetization curves collected via AGM measurements for all samples.

We fabricated thin films by co-sputter deposition [1] starting from pure high-resistive $NiFe_2O_4$ (NFO) ($\sim 160\,\mathrm{nm}$) up to the metallic $Ni_{33}Fe_{67}$ (10.4 nm) with intermediate $NiFe_2O_{x_1}$ (60 nm) and $NiFe_2O_{x_2}$ (35 nm), with $4 > x_1 > x_2 > 0$. The films were deposited on $MgAl_2O_4(001)$ (MAO) substrates by dc magnetron sputtering. The metallic film was deposited in Ar atmosphere with pressure in the range of $2 \cdot 10^{-3}$ mbar at room temperature (RT). The $NiFe_2O_{x_1}$ and $NiFe_2O_{x_2}$ films were prepared by reactive co-sputtering from an elemental Ni and Fe target in Ar and O_2 atmosphere at 610°C substrate temperature. For the $NiFe_2O_{x_1}$ bilayer the Ar partial pressure during the deposition was $1.7 \cdot 10^{-3}$ mbar, while the total pressure was $2 \cdot 10^{-3}$ mbar. For the $NiFe_2O_{x_2}$ bilayer the Ar partial pressure was $1.8 \cdot 10^{-3}$ mbar, while the total pressure was $2.3 \cdot 10^{-3}$ mbar. The pure NFO was grown in pure O_2 atmosphere with a pressure of $2 \cdot 10^{-3}$ mbar at 610°C substrate temperature. The base pressure in all cases was less than 10^{-8} mbar. Moreover, in the x-ray diffraction (XRD) patterns (partially shown in Ref. [2]), (004) Bragg peaks are visible for all samples unveiling a crystalline structure with epitaxial growth in [001] directions. The out-of-plane lattice constants are extracted from the XRD peaks to be equal to 8.44 Å, 8.40 Å and 8.33 Å for NFO, $NiFe_2O_{x_1}$

and $NiFe_2O_{x_2}$, respectively. Additionally, the in-plane lattice constants are identified from the position of the (606)-Peak ($2\theta \approx 103°$), which is observable with $\omega - 2\theta$ measurements and an ω-offset of $\Delta\omega \approx 45°$. Further structural information are discussed in Ref. [2].

Figure S1 illustrates the magnetization against the magnetic field extracted from alternating gradient magnetometry (AGM) measurements. The plots are presented after the subtraction of diamagnetic and paramagnetic contributions. In the magnetic field of 10 kOe, the $NiFe_2O_{x_1}$ and $NiFe_2O_{x_2}$ samples are clearly saturated. In contrast, for the NFO it is crucial to note that the magnetic saturation achieved in 10 kOe (which was the maximum field strength applied while measuring in the OPM configuration) was 80%, but this condition didn't affect the transport measurements since no ANE signal was detected in this configuration. The inset of Fig. S1 represents the magnetization curve of the $Ni_{33}Fe_{67}$ sample which already reached a saturation condition at around 3 kOe.

II. THEORETICAL AND EXPERIMENTAL BACKGROUND FOR XRMR

A fundamental theoretical background for the XRMR includes the determination of the optical properties of a material exposed to x-rays as given in the refractive index $n = 1 - \delta + i\beta$, where δ and β are the dispersion and the absorption coefficients, respectively, connected via the Kramers-Kronig relation. When the magnetization changes directions (±), the optical parameters δ and β vary by a fraction $\Delta\delta$ and $\Delta\beta$, respectively. These so called magnetooptic parameters are most pronounced at energies right around the absorption edge of the investigated material and vanish far from the resonance. Considering the interference of the reflected light from the surface and the interfaces this method can reveal a possible spin polarization in a film independent from the layer thickness [3].

Here, the XRMR data were collected at a fixed energy close to the Pt L_3 absorption edge by performing x-ray reflectivity (XRR) scans with circularly polarized x-rays (off-resonant at 11465 eV, resonant at 11565 eV) [4], while the field was switched between parallel and antiparallel orientation to the in-plane projection of the incident beam at every reflectivity angle. The degree of circular polarization was (88 ±1)% as derived from a model for the performance of the phase-plates [5].

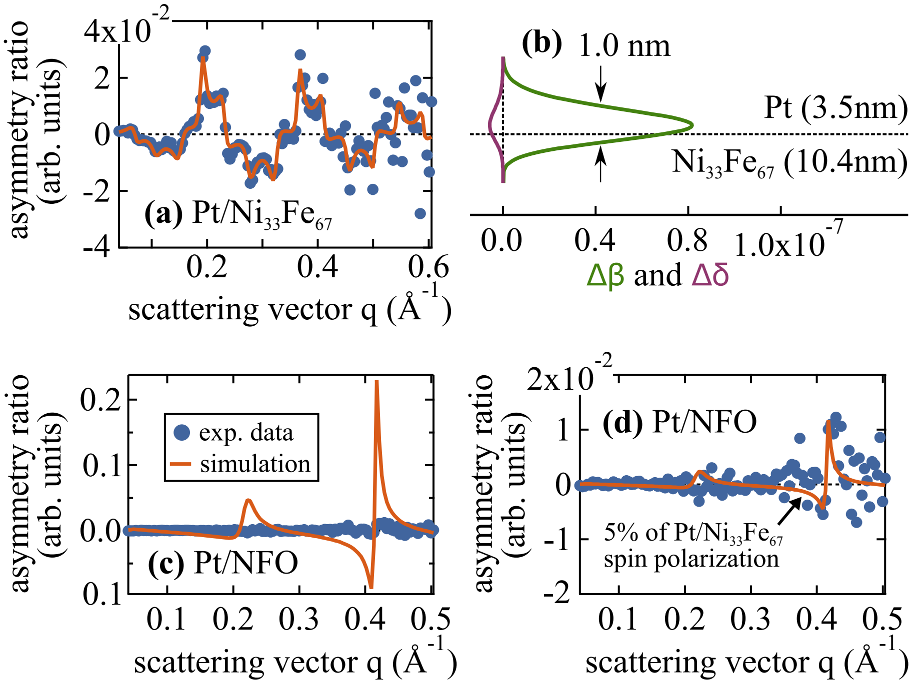

FIG. S 2. (a) XRMR asymmetry ratio for $Pt/Ni_{33}Fe_{67}$ and simulation with the corresponding magnetooptic depth profile (b). (c) XRMR asymmetry ratio for Pt/NFO after using the magnetooptic depth profile of (b), (d) close-up of the experimental data from (c) and simulation assuming 5% of the $Pt/Ni_{33}Fe_{67}$ spin polarization.

The fitting tool ReMagX [6] was used to evaluate the magnetic XRMR asymmetry ratio $\Delta I = \frac{I_+ - I_-}{I_+ + I_-}$ plotted over the scattering vector $q = \frac{4\pi}{\lambda} \sin\theta$, where λ: wavelength, $I_\pm$: XRR intensity for different field directions and θ: angle of incidence. The structural parameters (thickness, roughness) extracted from the fittings of the off-resonant XRR scans

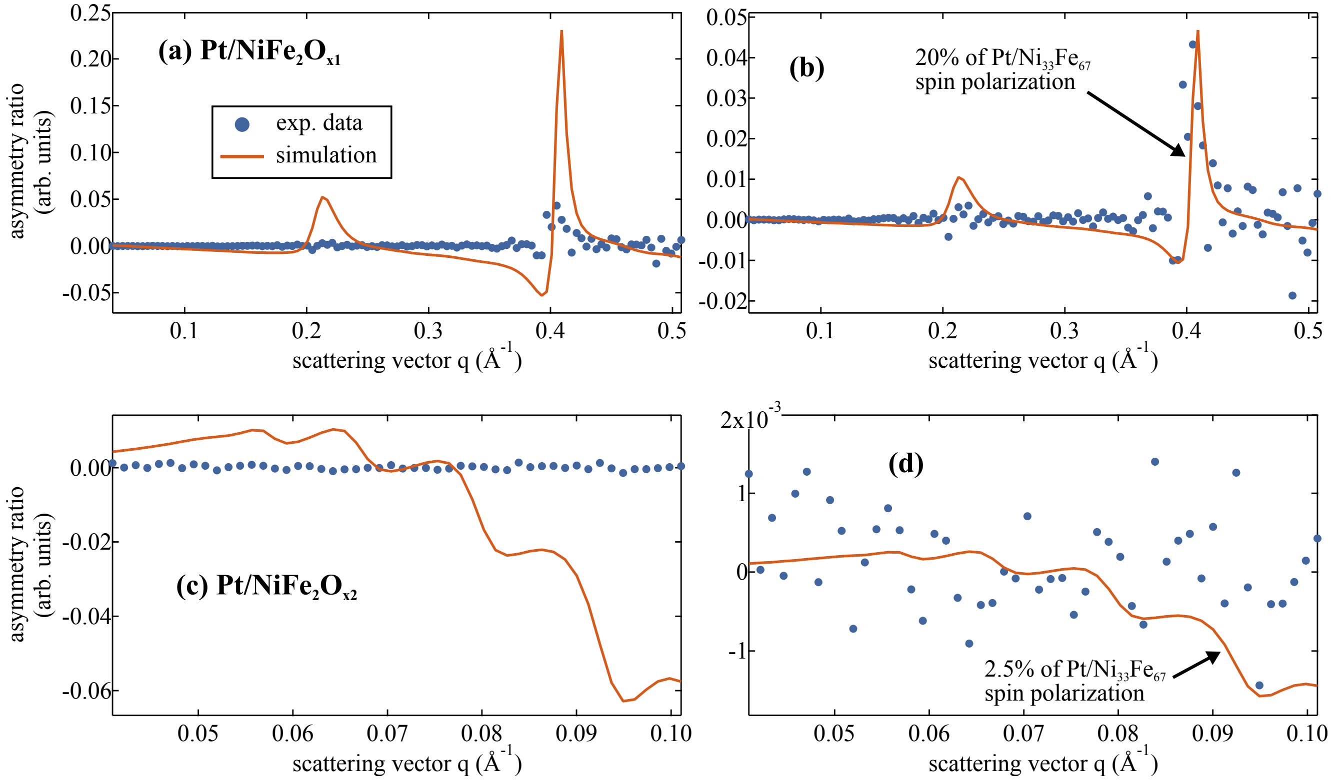

FIG. S 3. (a) XRMR asymmetry ratio for Pt/NiFe$_2$O$_{x_1}$ and simulation using the magnetooptic depth profile of the Pt/Ni$_{33}$Fe$_{67}$ bilayer, (b) assuming 20% of the Pt/Ni$_{33}$Fe$_{67}$ spin polarization. (c) XRMR asymmetry ratio for Pt/NiFe$_2$O$_{x_2}$ and simulation using the magnetooptic depth profile of the Pt/Ni$_{33}$Fe$_{67}$ bilayer, (d) assuming 2.5% of the Pt/Ni$_{33}$Fe$_{67}$ spin polarization.

using literature values for the optical parameters δ and β, are used to fit the resonant XRR curves and determine the optical parameters in resonance [7]. Afterwards, the XRMR asymmetry ratios are simulated using the previously derived parameters along with the variation of magnetooptic depth profiles for the magnetooptic parameters $\Delta\delta$ and $\Delta\beta$. The ratio $\frac{\Delta\beta}{\Delta\delta} = -14.3$ was kept fixed during fitting and was determined by adjusting the magnetooptic data from the *ab initio* calculations to a fixed q-scan [4]. We calculated this ratio at an energy of 11565 eV where we also collected our XRMR measurements. Finally, by comparing the resulting $\Delta\delta$ and $\Delta\beta$ values to optical data from *ab initio* calculations [3], the magnetic moment per spin polarized Pt atom is identified.

In Fig. S2 the measured XRMR asymmetry ratio and the corresponding simulation are presented for the Pt/Ni$_{33}$Fe$_{67}$ and Pt/NFO bilayers using the corresponding magnetooptic depth profile for the metallic sample. In Fig. S2(a) the measured XRMR asymmetry ratio for the Pt/Ni$_{33}$Fe$_{67}$ bilayer is displayed. From the corresponding fitting and by comparing the experimental fit values of $\Delta\delta$ and $\Delta\beta$ derived from the magnetooptic depth profile in Fig. S2(b) to *ab initio* calculations [3] we obtain a maximum Pt magnetic moment of $(0.48 \pm 0.08)\,\mu_B$ per spin polarized Pt atom. In Fig. S2(c) the measured XRMR asymmetry ratio for the Pt/NFO bilayer is presented along with a simulation using a magnetooptic depth profile identical to the one derived for the Pt/Ni$_{33}$Fe$_{67}$ bilayer. Obviously, the simulated asymmetry ratio of the Pt/NFO sample (Fig. S2(c)) deviates strongly from the one of the Pt/Ni$_{33}$Fe$_{67}$ sample (Fig. S2(a)), although the same magnetooptic depth profile (Fig. S2(b)) was used. This is due to the different optical constants of Ni$_{33}$Fe$_{67}$ and NFO. Since no asymmetry was detected for the Pt/NFO sample, a potential MPE present in this film must be significantly smaller than in the all-metallic system. By decreasing the magnitude of the magnetooptic parameters down to 5% of the Pt/Ni$_{33}$Fe$_{67}$ spin polarization (Fig. S2(d)), we can estimate a detection limit leading to an upper limit for the maximum magnetic moment in Pt of $0.04\,\mu_B$ per spin polarized Pt atom.

In Fig. S3 the measured XRMR asymmetry ratio is presented for the Pt/NiFe$_2$O$_{x_1}$ (Fig. S3(a),(b)) and Pt/NiFe$_2$O$_{x_2}$ bilayers (Fig. S3(c),(d)), respectively, along with a simulation using a magnetooptic depth profile identical to the one derived for the Pt/Ni$_{33}$Fe$_{67}$ bilayer. Firstly, we compare the experimental data with an asymmetry ratio simulation that describes a Pt/NiFe$_2$O$_x$ system but with the same magnetooptic depth profile as for Pt/Ni$_{33}$Fe$_{67}$. As in the case of the Pt/NFO analyzed previously, the simulated asymmetry ratio of the Pt/NiFe$_2$O$_{x_1}$ (Fig. S3(a)) deviates strongly from the one of the Pt/Ni$_{33}$Fe$_{67}$ sample, although the same magnetooptic depth profile was used (Fig. S2(b)), due to the different optical constants of $Ni_{33}Fe_{67}$ and $NiFe_2O_{x_1}$. Therefore, since the simulated asymmetry ratio of the Pt/$NiFe_2O_{x_1}$ sample does not match the experimental data, a potential MPE present in this film must be significantly smaller than in the all-metallic system. In order to extract a limit for a quantitative magnetic moment value, we decreased the magnitude of the magnetooptic parameters down to 20% of the Pt/$Ni_{33}Fe_{67}$ spin polarization (Fig. S3(b)) and, thus, we estimated a detection limit leading to an upper limit for the maximum magnetic moment in Pt of 0.1 μ_B per spin polarized Pt atom. Accordingly, for the Pt/$NiFe_2O_{x_2}$ bilayer we decreased the magnitude of the magnetooptic parameters down to 2.5% of the Pt/$Ni_{33}Fe_{67}$ spin polarization (Fig. S3(d)) and we estimated a detection limit leading to an upper limit for the maximum magnetic moment in Pt of 0.01 μ_B per spin polarized Pt atom. The extracted limits for both samples are different compared to Pt/NFO due to different signal-to-noise ratios in the XRMR data.

III. APPLICATION OF THERMAL GRADIENTS

In the IPM geometry the samples were clamped between two copper blocks from their top and bottom sides. The copper block on the top side acted as a heat source and the one on the bottom side acted as a heat sink. In between the upper copper block and the sample there was an additional magnesium oxide layer with a thickness of 0.5 mm in order prevent electrical contacting between those two parts. In between the lower copper block and the bottom side of the film a Peltier element was placed acting as a heat flux sensor. Then, an out-of-plane thermal gradient was homogeneously applied to the film in a presence of an in-plane magnetic field. The temperature difference between the two copper blocks was measured by two K-type thermocouples.

In the OPM geometry the samples were placed on top of two copper blocks and were clamped with copper plates on top in the hot side. Therefore, we could ensure a homogeneous application of an in-plane thermal gradient in a presence of an out-of-plane field. In the cold side a Peltier element was placed between the sample and the copper block for the detection of the heat flux.

The measurements were performed in vacuum at room temperature. For the voltage measurements two aluminum wires 25 μm thick were bonded on top of the samples and glued properly with silver paste to copper wires that are connected to the electrical feedthroughs of the vacuum chamber.

IV. HEAT FLUX CALCULATION

To calculate the heat flux ϕ_q in the IPM geometry we inserted Peltier elements as heat flux sensors right below the samples and converted the output signal of the sensor into heat flux by taking into account the cross section area of the heat between the sample and the Peltier element. We calibrated the heat flux sensors by using an electric heater resistor to simulate a Joule heat source as described by Sola *et al.* [8, 9]. In the OPM configuration, the heat flux was theoretically determined by taking into account the thermal conductivity of the FM layers. For the Pt/$Ni_{33}Fe_{67}$ bilayer we additionally considered the contribution of the spin polarized layer of Pt with the effective spin polarized thickness extracted from the XRMR investigations.

The heat Q which passes through every layer of the samples is calculated from

$$Q = \frac{\Delta T}{L_T} K \cdot S \tag{1}$$

where L_T: total length of the sample in the direction of the temperature gradient, S: side area perpendicular to the direction of the heat propagation and K: thermal conductivity of the corresponding layer. The ΔT is extracted from the value of the thermal conductivity of the MAO substrate which is 24 $Wm^{-1}K^{-1}$ [10] and the heat flux output taken from a Peltier element located below the substrate. We consider that the ΔT remains the same along all the layers. The main contribution to the total heat of the sample comes from the MAO layer since this is the thickest part of every sample. However, we are only interested in the contribution of the FM layer in which the effects are generated. The thermal conductivities of the $NiFe_2O_x$ $(x > 0)$ layers are assumed to be (8.5 ± 0.9) $Wm^{-1}K^{-1}$ [11], since all of these samples are in the insulating regime at RT. The error is introduced since the absolute value of the thermal conductivity corresponds to a bulk material and not to thin films. Then the heat flux is determined from

$$\phi_q = \frac{K\,\Delta T}{L_T} \quad . \tag{2}$$

It is crucial to also consider the contribution of the spin polarized Pt layer to the heat flux in the case that an MPE is present. This has to be examined only for the Pt/$Ni_{33}Fe_{67}$ bilayer as confirmed by XRMR. In this case $K_{\mathrm{Ni_{33}Fe_{67}}}$ consists of two components

$$K_{\mathrm{Ni_{33}Fe_{67}}} = K_{\mathrm{e}} + K_{\mathrm{ph}} \tag{3}$$

where K_{e}: thermal conductivity of free electrons and K_{ph}: thermal conductivity of phonons. The value of K_{e} is calculated from the Wiedemann-Franz law

$$K_{\mathrm{e}} = L\,\sigma\,T \tag{4}$$

where σ: measured electrical conductivity at each temperature T and L=$2.44 \cdot 10^{-8}\,\mathrm{W\Omega K^{-2}}$ is the Lorentz number. The value of K_{ph} is regarded to be equal to $(8.5\pm0.9)\,\mathrm{Wm^{-1}K^{-1}}$. The contribution from the 1.0 nm spin polarized layer of Pt is quantified to be 17% of the heat flux of the $Ni_{33}Fe_{67}$ layer. The chosen heat flux values for the normalization of the measured voltage in Fig. 2 of the main text are comparable but not identical. However, the magnitude of the normalized signal will not be influenced by the choice of the heat flux value due to the linear interdependency between both the voltage and the heat flux.

V. PHYSICAL CHARACTERISTICS OF THE SAMPLES

In the Table I the measured physical parameters of all samples are presented, where t_{FM}: thickness of the FM, t_{Pt}: thickness of the Pt layer, $t_{\mathrm{Pt}}^{\mathrm{NM}}$: thickness of the non-magnetic fraction of Pt, $t_{\mathrm{Pt}}^{\mathrm{SP}}$: thickness of the spin polarized fraction of Pt, ρ_{FM}: electrical resistivity of the FM (measured on the samples without Pt on top), ρ_{Pt}: electrical resistivity of Pt and R: resistance between the voltage contacts, for each film respectively. The ρ_{Pt} values were calculated from the measured ρ values of the twin samples with and without the Pt layer on top.

Film	Pt/NFO	Pt/$NiFe_2O_{x_1}$	Pt/$NiFe_2O_{x_2}$	Pt/$Ni_{33}Fe_{67}$
t_{FM} (nm)	160	60	35	10.4
t_{Pt} (nm)	3.0	2.7	3.1	3.5
$t_{\mathrm{Pt}}^{\mathrm{NM}}$ (nm)	3.0	2.7	3.1	2.5
$t_{\mathrm{Pt}}^{\mathrm{SP}}$ (nm)	0.0	0.0	0.0	1.0
ρ_{FM} (Ωm)	40.5	$1.5 \cdot 10^{-4}$	$4.5 \cdot 10^{-5}$	$4.2 \cdot 10^{-7}$
ρ_{Pt} (Ωm)	$1.6 \cdot 10^{-7}$	$1.7 \cdot 10^{-7}$	$1.8 \cdot 10^{-7}$	$1.6 \cdot 10^{-7}$
R_{FM} (Ω)	$3.4 \cdot 10^{9}$	$3.3 \cdot 10^{4}$	$1.7 \cdot 10^{4}$	$0.5 \cdot 10^{3}$

TABLE I. Resistivity at room temperature, thickness and resistance between the voltage contacts for Pt/NFO, Pt/$NiFe_2O_{x_1}$, Pt/$NiFe_2O_{x_2}$, and Pt/$Ni_{33}Fe_{67}$ samples.

As additional information the Seebeck coefficients for the $NiFe_2O_{x_1}$, $NiFe_2O_{x_2}$ and $Ni_{33}Fe_{67}$ are found to be equal to: $57.2\,\mu$V/K, $28.2\,\mu$V/K and $18.2\,\mu$V/K, correspondingly. The Seebeck coefficients are estimated after the subtraction of the contribution from the gold wires used for the electrical contacts [12]. Moreover, the $D_{\mathrm{ANE^{FM}}}$ coefficients for $NiFe_2O_{x_1}$, $NiFe_2O_{x_2}$ and $Ni_{33}Fe_{67}$ are also calculated in units V/K and found to be equal to: 2.8 nV/K, 3.8 nV/K and 4.7 nV/K, respectively. The ANE coefficient for the metallic sample is consistent with values found for permalloy in earlier publications [13].

Figure S4 represents the change of RT resistivity according to the partial O_2 pressure during deposition. The partial O_2 pressure was calculated from the partial Ar pressures and total pressures recorded during the deposition of each sample. A clear increase of the resistivity is observed when the amount of oxygen increases.

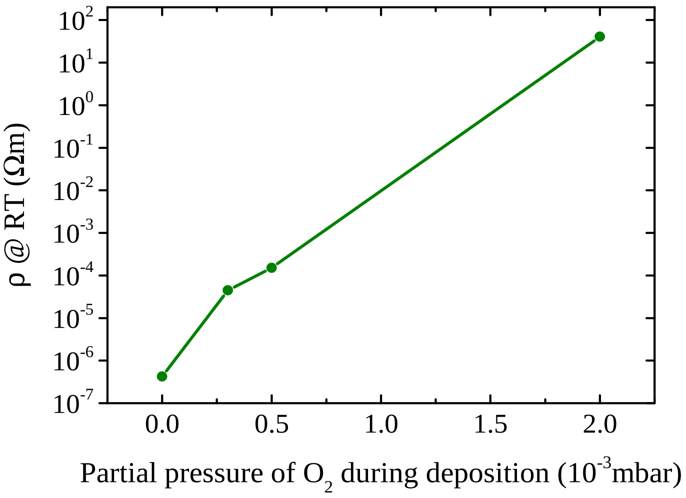

FIG. S 4. Resistivity measured at RT for the corresponding partial O_2 pressure of all samples.

VI. PARASITIC PLANAR NERNST AND TRANSVERSE SPIN SEEBECK EFFECT CONTRIBUTIONS IN THE OPM CONFIGURATION

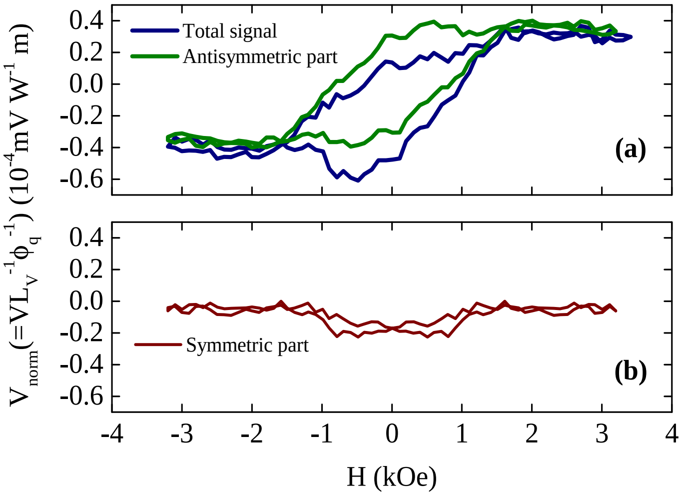

FIG. S 5. (a) Total ANE^{FM} + ANE^{prox} signal and antisymmetric contribution of it for the Pt/$Ni_{33}Fe_{67}$ bilayer. (b) The symmetric contribution to the total signal.

In the OPM configuration the application of an in-plane thermal gradient is combined with the application of an out-of-plane magnetic field and an unintended misalignment of the field direction (possible in-plane components) could induce parasitic contributions hampering the measured signal. One possible contribution could be the transverse spin Seebeck effect (TSSE) which is controversially discussed. So far, in our former investigations we could not observe any evidence for the existence of a TSSE and, therefore, we neglect such a parasitic signal in our measurements [14–17]. These results are in line with prior publications [18, 19].

Furthermore, apart from the TSSE an additional planar Nernst effect (PNE) contribution could contaminate the measured voltage prohibiting from the correct interpretation of the desired signal. This contribution is indeed observable while measuring on the Pt/$Ni_{33}Fe_{67}$ sample and appears in the deep of the curve in Fig. 2(d) of the main manuscript. However, the PNE is symmetric with the field and we can easily separate this contribution from the antisymmetric ANE signal. In Fig. S5(a) the total signal is presented together with the extracted antisymmetric contribution from the ANE. In Fig. S5(b) the symmetric contribution is illustrated which is considerably smaller than the antisymmetric one. In addition, since we are interested in the difference of voltages between plus and minus magnetic field saturation the symmetric signal does not contribute to the measured voltage and the values extracted from the antisymmetric signal are the same as if we calculate the magnitude of the effect from the total one. Therefore, we conclude that although a PNE contribution is visible in our measurements, it doesn't affect the magnitude of the effect allowing for the correct interpretation of the measured voltage.

VII. THICKNESS DEPENDENCY OF SSE AND ANE$^{\mathrm{FM}}$ COEFFICIENTS

A challenging issue is the thickness dependency of the obtained SSE and ANE$^{\mathrm{FM}}$ coefficients. In order to further elucidate this issue we disentangled the effects and extracted the corresponding SSE and ANE$^{\mathrm{FM}}$ coefficients for an additional Pt/NFO and Pt/$\mathrm{Ni_{33}Fe_{67}}$ sample with nominal FM thicknesses equal to t_{NFO}=22 nm and $t_{\mathrm{Ni_{33}Fe_{67}}}$=160 nm. For both samples t_{Pt}=3 nm. As visible from Fig. S6 the SSE coefficient of the additional NFO sample (rhombus) is smaller then the initial one illustrating a weak thickness dependency. However, the main trend of decreasing S_{SSE} with increasing conductivity still holds. Moreover, considering the additional Pt/$\mathrm{Ni_{33}Fe_{67}}$ bilayer (triangle) a weaker thickness dependency of both coefficients can be extracted. Consequently, the $D_{\mathrm{ANE^{FM}}}$ clearly increases with increasing conductivity whereas the S_{SSE} decreases. These results, are a first step towards the study of the thickness dependency of SSE and ANE$^{\mathrm{FM}}$ coefficients in such systems and further investigation should be conducted to clarify this issue.

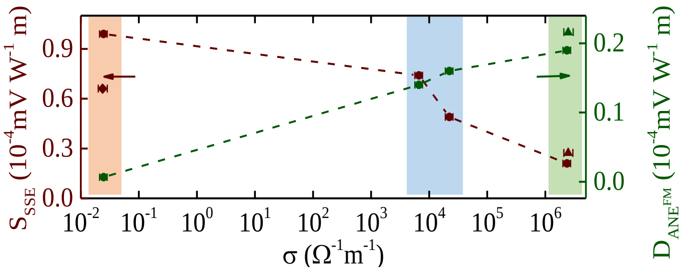

FIG. S 6. SSE and ANE$^{\mathrm{FM}}$ coefficients as a function of the electrical conductivity σ for $\mathrm{NiFe_2O}_{x_1/x_2}$ (blue area), NFO (orange area) and $\mathrm{Ni_{33}Fe_{67}}$ (green area) samples.

VIII. BAND GAP ENERGY DETERMINATION

The optical band gap energies are obtained from ultraviolet-visible spectroscopy, and in that respect extracted using Tauc plots [1] ($(\alpha E)^{0.5}$ versus energy), where α(E) is the absorption coefficient extracted from the measured transmission T and reflectance R spectra by $\alpha = \frac{1}{d} \ln \frac{1-R}{T}$, where d is the thickness of the corresponding $\mathrm{NiFe_2O}_x$ ($x > 0$) layer. The optical band gap for the NFO film is estimated to be $E_{\mathrm{gap}}^{\mathrm{NFO}} \approx 1.49$ eV, close to our previous investigations [1]. The optical band gap for the $\mathrm{NiFe_2O}_{x_1}$ and $\mathrm{NiFe_2O}_{x_2}$ sample is $E_{\mathrm{gap}}^{\mathrm{NiFe_2O}_{x_1}} \approx 1.27$ eV and $E_{\mathrm{gap}}^{\mathrm{NiFe_2O}_{x_2}} \approx 1.09$ eV, respectively, unveiling the more conducting character of the latter. A detailed band gap analysis on these $\mathrm{NiFe_2O}_x$ ($x > 0$) samples is reported in Ref. [2]. However, the use of Tauc plots for the determination of the band gap energies could lead to rough estimated values because of the uncertainties that may come up during this kind of data processing [20]. The electrical band gap for the NFO determined from an activated conduction is equal to 0.19 eV [2] in accordance with previous publications [1, 21, 22].

[1] C. Klewe, M. Meinert, A. Boehnke, K. Kuepper, E. Arenholz, A. Gupta, J.-M. Schmalhorst, T. Kuschel, and G. Reiss, J. Appl. Phys. **115**, 123903 (2014).

[2] P. Bougiatioti, O. Manos, C. Klewe, D. Meier, N. Teichert, J.-M. Schmalhorst, T. Kuschel, and G. Reiss, arXiv:1708.01937 (2017).

[3] T. Kuschel, C. Klewe, J.-M. Schmalhorst, F. Bertram, O. Kuschel, T. Schemme, J. Wollschläger, S. Francoual, J. Strempfer, A. Gupta, M. Meinert, G. Götz, D. Meier, and G. Reiss, Phys. Rev. Lett. **115**, 097401 (2015).

[4] T. Kuschel, C. Klewe, P. Bougiatioti, O. Kuschel, J. Wollschläger, L. Bouchenoire, S. D. Brown, J. M. Schmalhorst, D. Meier, and G. Reiss, IEEE Trans. Magn. **52**, 4500104 (2016).

[5] L. Bouchenoire, S. D. Brown, P. Thompson, J. A. Duffy, J. W. Taylor, and M. J. Cooper, J. Synchrotron Radiat. **10**, 172 (2003).

[6] S. Macke and E. Goering, J. Phys.: Condens. Matter **26**, 363201 (2014).

[7] C. Klewe, T. Kuschel, J.-M. Schmalhorst, F. Bertram, O. Kuschel, J. Wollschläger, J. Strempfer, M. Meinert, and G. Reiss, Phys. Rev. B **93**, 214440 (2016).

[8] A. Sola, M. Kuepferling, V. Basso, M. Pasquale, T. Kikkawa, K. Uchida, and E. Saitoh, J. Appl. Phys. **117**, 17C510 (2015).

[9] A. Sola, P. Bougiatioti, M. Kuepferling, D. Meier, G. Reiss, M. Pasquale, T. Kuschel, and V. Basso, Sci. Rep. **7**, 46752 (2017).

[10] B. Schulz and M. Hoffmann, High Temp. - High Pressures **34**, 203 (2002).

[11] A. T. Nelson, J. T. White, D. A. Andersson, J. A. Aguiar, K. J. McClellan, D. D. Byler, M. P. Short, and C. R. Stanek, J. Am. Ceram. Soc. **97**, 1559 (2014).

[12] O. Reimer, D. Meier, M. Bovender, L. Helmich, J.-O. Dreessen, J. Krieft, A. S. Shestakov, C. H. Back, J.-M. Schmalhorst, A. Hütten, G. Reiss, and T. Kuschel, Sci. Rep. **7**, 40586 (2017).

[13] J. Holanda, O. Alves Santos, R. O. Cunha, J. B. S. Mendes, R. L. Rodríguez-Suárez, A. Azevedo, and S. M. Rezende, Phys. Rev. B **95**, 214421 (2017).

[14] D. Meier, D. Reinhardt, M. Schmid, C. H. Back, J.-M. Schmalhorst, T. Kuschel, and G. Reiss, Phys. Rev. B **88**, 184425 (2013).

[15] M. Schmid, S. Srichandan, D. Meier, T. Kuschel, J.-M. Schmalhorst, M. Vogel, G. Reiss, C. Strunk, and C. H. Back, Phys. Rev. Lett. **111**, 187201 (2013).

[16] D. Meier, D. Reinhardt, M. van Straaten, C. Klewe, M. Althammer, M. Schreier, S. T. B. Goennenwein, A. Gupta, M. Schmid, C. H. Back, J.-M. Schmalhorst, T. Kuschel, and G. Reiss, Nat. Commun. **6**, 8211 (2015).

[17] A. S. Shestakov, M. Schmid, D. Meier, T. Kuschel, and C. H. Back, Phys. Rev. B **92**, 224425 (2015).

[18] S. Y. Huang, W. G. Wang, S. F. Lee, J. Kwo, and C. L. Chien, Phys. Rev. Lett. **107**, 216604 (2011).

[19] A. D. Avery, M. R. Pufall, and B. L. Zink, Phys. Rev. Lett. **109**, 196602 (2012).

[20] M. Meinert and G. Reiss, J. Phys.: Condens. Matter **26**, 115503 (2014).

[21] H. Lord and R. Parker, Nature **188**, 929 (1960).

[22] D. Meier, T. Kuschel, L. Shen, A. Gupta, T. Kikkawa, K. Uchida, E. Saitoh, J.-M. Schmalhorst, and G. Reiss, Phys. Rev. B **87**, 054421 (2013).